THE JOURNAL OF PHYSICAL CHEMISTRY C

ARTICLE

pubs.acs.org/JPCC

$(Sn,Al)O_x$ Films Grown by Atomic Layer Deposition

Jaeyeong Heo, Yiqun Liu, Prasert Sinsermsuksakul, Zhefeng Li, Leizhi Sun, Wontae Noh, and Roy G. Gordon*

Department of Chemistry and Chemical Biology, Harvard University, Cambridge, Massachusetts 02138, United States

ABSTRACT: $(Sn,Al)O_x$ composite films with various aluminum (Al) to tin (Sn) ratios were deposited using an atomic layer deposition technique. The chemisorption behavior of cyclic amide of tin(II) and trimethylaluminum were analyzed by Rutherford backscattering spectroscopy. Both precursors showed retarded and enhanced chemisorption on Al_2O_3 and SnO_2 surfaces, respectively. The films show highly anisotropic electrical conductivity, i.e., much higher resistivity in the direction through the film than parallel to the surface of the film. The cause of the anisotropy was investigated by cross-sectional transmission electron microscopy, which showed a nanolaminate structure of crystalline SnO_2 grains separated by thin, amorphous Al_2O_3 monolayers. When the Al concentration was higher than ~35 atom %, the composite films became amorphous, and the vertical and lateral direction resistivity values converged toward one value. By properly choosing the ratio of SnO_2 and Al_2O_3 subcycles, controlled adjustment of film electrical resistivity over more than 15 orders of magnitude was successfully demonstrated.

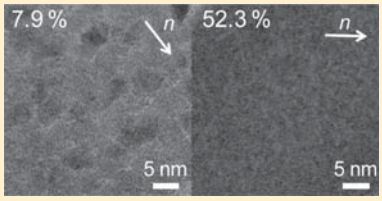

I. INTRODUCTION

Tin oxide (SnO_2) is a transparent semiconductor with a wide band gap and electrical resistivity as low as 2×10^{-4} Ω·cm and high infrared reflectivity, over 90%.[1−4] These properties are achieved using n-type doping by substituting fluorine for about 1% of the oxygen.[5] The low electrical resistance and optical transparency in SnO_2 are widely used in applications such as solar cells, displays, touch controls, and defrosting windows.[6,7] Its high infrared reflectivity provides its energy saving properties in low-emissivity windows.[8] Some potential applications of SnO_2 would require high instead of low electrical resistance. For example, transparent thin film transistors for displays,[9−11] microchannel electron multiplier plates,[12−14] and hole-blocking layers in solar cells[15] would require highly resistive SnO_2 layers that still maintain high electron mobility. Native defects, such as oxygen vacancies and hydroxyl groups, normally contribute electrons to the conduction band. However, high resistivity requires a low concentration of electrons in the conduction band, so electrons from these native defects need to be trapped in order to obtain highly resistive SnO_2. Electrons could be trapped by substituting nitrogen for oxygen, or substituting trivalent metals for tin. In this paper, we took the latter approach, and substituted aluminum (Al^{3+}) for tin (Sn^{4+}). Thus by adding insulating Al_2O_3 into SnO_2, we explored the possibility of controlling its film resistivity over a wide range, forming $(Sn,Al)O_x$ composite materials. One advantage of using Al_2O_3 for modulation of the conducting layer is that it can also be used as the electron emission layer in a microchannel electron multiplier plate.[13]

Atomic layer deposition (ALD) can produce multicomponent films with good control of their stoichiometry. This control of stoichiometry even extends to highly conformal films on complex structures with high aspect ratios, such as narrow holes. ALD involves sequential and self-limiting chemical reactions of precursor pulses on the surface of a growing film.[16−22] As a result, the films can be extremely smooth and continuous without pinholes. These unique characteristics have made ALD one of the most popular techniques for new application areas of various nanotechnologies.[23−25] Multicomponent ALD with the use of more than two cation precursors involves repetitive exposure of different precursors to heterogeneous surfaces. Differing chemisorption amounts of precursors on different oxide surfaces make it difficult to predict the composition of the films.[26−29] Therefore, in-depth understanding of chemisorption of precursors on heterogeneous surfaces is necessary to control the composition and the electrical, optical, magnetic, and mechanical properties of the resulting films.[29−34]

One process for ALD of SnO_2 at low temperature has been reported, but the films were amorphous as deposited, and needed a high-temperature anneal to obtain crystalline material with significant mobility.[35] A recently reported ALD process overcomes this difficulty by using a more reactive tin source that deposits well-crystallized SnO_2 films with reasonably high electron mobility at temperatures as low as 100 °C.[36]

There have been several efforts to investigate the chemisorption behavior of trimethylaluminum ($Al(CH_3)_3$, TMA) on ZnO[29,32−34,37] and TiO_2[30] surfaces. Elam et al. reported retarded nucleation of both diethylzinc ($Zn(CH_2CH_3)_2$, DEZ) and TMA following the other subcycles by using in situ quartz crystal microbalance and additional ex situ measurements of film properties.[29,32] Na et al. conducted a similar experiment on Al-doped ZnO and also confirmed the retarded nucleation of DEZ on Al_2O_3 surfaces.[33] For TiO_2 films, Kim et al. reported retarded adsorption of titanium tetrakis(isopropoxide), $Ti(O\text{-}i\text{-}C_3H_7)_4$,

Received: March 8, 2011
Revised: April 8, 2011
Published: April 28, 2011

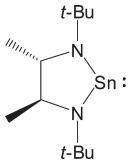

Figure 1. Molecular structure of CAT precursor 1,3-bis(1,1-dimethylethyl)-4,5-dimethyl-(4*R*,5*R*)-1,3,2-diazastannolidin-2-ylidene.

(TTIP) on Al_2O_3 surfaces and observed enhanced chemisorption of TMA on TiO_2 surfaces.[30]

Here, we report enhanced chemisorption of TMA on SnO_2 surfaces by using Rutherford backscattering spectroscopy (RBS) for analysis of films with various Sn to Al ratios. Hydrogen peroxide (H_2O_2) was used as the oxygen source. After the first subcycle of TMA−H_2O_2 on a SnO_2 surface, the chemisorption of the next TMA dose was reduced to its usual value on Al_2O_3. This result suggests that one subcycle of TMA−H_2O_2 almost completes one monolayer formation of Al_2O_3 on a SnO_2 surface. Electrical anisotropy of the films was revealed by comparison of resistance measurements in the vertical and lateral directions. This anisotropy was correlated with the microstructure of the composite films revealed by transmission electron microscopy (TEM). By properly controlling the number of SnO_2 and Al_2O_3 cycles, the film's resistivity could be controlled over more than 15 orders of magnitude. The present study provides important insight into the chemisorption behaviors of ALD precursors on heterogeneous surfaces and their correlation with the electrical and microstructural properties of composite materials.

II. EXPERIMENTAL PROCEDURE

$(Sn,Al)O_x$ thin films were formed using a custom-built hot-wall ALD reactor (volume = 0.627 L) at growth temperature of 120 °C. A cyclic amide of tin (CAT), 1,3-bis(1,1-dimethylethyl)-4,5-dimethyl-(4*R*,5*R*)-1,3,2-diazastannolidin-2-ylidene, was used as a precursor for tin.[36] Figure 1 shows its molecular structure. CAT was sublimed at 40 °C for purification, at which temperature it has a vapor pressure of 0.42 Torr. The oxygen precursor was vapor from 50 wt % hydrogen peroxide (H_2O_2, Sigma Aldrich) kept at room temperature. Three doses of CAT and H_2O_2 were required for saturation of the growth rate for SnO_2, corresponding to total exposures of 1.9 and 1.5 Torr·s, respectively. The saturated growth rate for SnO_2 was ~0.175 nm/cycle, as reported elsewhere.[36] The purge time after each dose was set to be 25 and 45 s, respectively. TMA (Sigma Aldrich) was used as the Al precursor. It was kept at room temperature, vaporized into a trap volume (~3 mL) made of stainless steel and subsequently delivered to the reaction chamber by using pneumatic valves. Two doses for both TMA and H_2O_2 were enough to obtain saturated growth (~0.1 nm/cycle) of Al_2O_3 at 120 °C, corresponding to total exposures of 0.24 Torr·s for TMA and 0.17 Torr·s for H_2O_2. Exposure of 0.01−0.1 Torr·s for both TMA and H_2O is known to be sufficient to obtain saturation of the film surface in the TMA−H_2O ALD process.[38] This saturated growth per cycle is similar to the value reported by Kumagai et al., who used the same precursors (TMA/H_2O_2).[39] Purge time for both TMA and H_2O_2 precursors was set to 60 s to completely remove excess precursor vapor and prevent any gas-phase reactions.

The $(Sn,Al)O_x$ composite growth sequence consists of n subcycles of SnO_2, followed by l subcycles of Al_2O_3, making one complete supercycle. Each subcycle consists of Sn (or Al) dose/purge/H_2O_2 dose/purge steps. The SnO_2/Al_2O_3 supercycle was repeated by m times. Here, the following notation is used for convenience in this study: $m(n,l)$ where m, n, and l represent the total number of repetitions of the supercycle, the total number of SnO_2 and Al_2O_3 subcycles, respectively. Total growth cycles $[m(n+l)]$ were set to be 300 cycles except for AlO_x growth where 400 cycles were used. 60(3,2) and 60(2,3) sequences were used for the high Al atomic concentrations. $m(n,1)$ sequences were used for targeting $(Sn,Al)O_x$ with less aluminum. Table 1 summarizes all the sequences that were used in the present study in addition to their measured Al atomic percentages, calculated ones, film densities, and refractive indices.

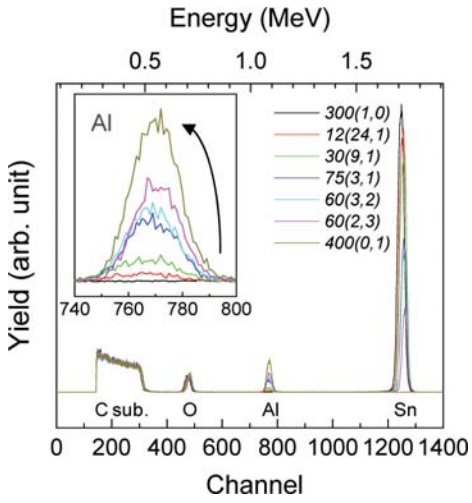

Figure 2. Rutherford backscattering spectra of $(Sn,Al)O_x$ composite films with various Al to Sn concentrations. The Al peaks are enlarged as an inset. The intensity of the Al peaks increases with increasing the percentage of Al_2O_3 subcycle. The notation $m(n,l)$ was used where m, n, and l represent total repetitions, the number of SnO_2 subcycle, and the number of Al_2O_3 subcycle, respectively. Total growth cycles were set to close to 300 cycles except 400 cycles for pure Al_2O_3 growth for comparison.

The number of chemisorbed Al atoms per growth cycle and composition of the films were evaluated from ex situ RBS analysis using 2 MeV He^{2+} beam. Glassy carbon (Alfa Aesar) was used as a substrate for RBS analysis, which enables the detection of O and Al peaks separated from the substrate background. The simulation error for atomic density was less than 3%, which gives less than ±1.5 atom % variation in calculated Al concentrations. The carbon substrate was cleaned with 10% aqueous HF (5 s), deionized water (30 s), and isopropanol (10 s) prior to drying and ultraviolet−ozone cleaning for 3 min to facilitate the initiation of the film growth.[36] The areal density of oxygen for an ultraviolet−ozone treated carbon substrate was measured to be ~2 × 10^{14} atoms/cm^2, which does not affect the oxygen signal which comes from a grown oxide film. The film density was calculated using the total mass of Sn, Al, and O atoms from RBS analysis and the film thickness obtained from X-ray reflectivity (XRR, Scintag, XDS 2000). High-resolution TEM (HRTEM, Jeol, JEM-2100) was employed for evaluation of the microstructures of the films.

Lateral-direction film resistivity was evaluated from a four-point probe (Veeco Instruments, FPP-100) and circular transmission line measurements.[40,41] By using the circular transmission line method (inner radius, 50 μm; outer radii, 54−100 μm),

Table 1. Physical Properties of $(Sn,Al)O_x$ Composite Films for Different Growth Sequences

$m(n, l)$	Al (atom %) from rule of mixture	Al (atom %) from RBS	Al (atom %) from model	density (g/cm^3)	refractive index
300(1,0)	0	0	0	5.83	1.98
12(24,1)	3.7	7.9	8.0	5.21	1.97
30(9,1)	9.2	20.4	20.4	5.03	1.90
33(8,1)	10.2	24.5	22.7	4.85	1.82
38(7,1)	11.5	27.1	25.7	4.82	1.79
75(3,1)	23.3	52.3	52.3	3.67	1.73
60(3,2)	37.8	58.6	61.6	3.63	1.73
60(2,3)	57.8	76.5	79.1	3.13	1.69
400(0,1)	100.0	100.0	100	2.83	1.63

we were able to measure sheet resistance of films up to $\sim 10^{10}$ Ω/square. Indium was used for Ohmic contacts.[42] $I-V$ measurements were also performed to study the vertical electron flow through the film in order to estimate the thickness-normal resistivity. For the $I-V$ measurements, films were deposited on HF-cleaned highly doped n-type Si substrates and 30 nm/2 nm thick Au/Cr top electrodes were formed with a shadow mask in an e-beam evaporator (Sharon). The measurement of film thickness and refractive index was performed by spectroscopic ellipsometry (Woollam, WVASE32), and some films were cross-checked by XRR and TEM. Surface morphology of the deposited films was investigated by using atomic force microscopy (AFM, Asylum, MFP-3D SA). Water contact angle measurement (ChemInstruments, CAM-Plus) was performed to study the hydrophilicity of the films.

III. RESULTS AND DISCUSSION

Figure 2 shows RBS spectra of $(Sn,Al)O_x$ composite films grown on glassy carbon substrates. The peaks at the channel numbers of 1270, 783, 495, and 328 were assigned to Sn, Al, O, and C, respectively. No other peaks were detected. The inset expands the Al peaks in more detail. The peak Al intensity increases as the number of Al_2O_3 subcycles increases. The Al signal is at the noise level when no Al_2O_3 subcycle is used [300(1,0)]. The Sn peak follows the opposite trend to the Al peak and its intensity increases as the number of SnO_2 subcycles increases.

Panels a and b of Figure 3 show the measured Sn and Al content as a function of the relative percentage of SnO_2 and Al_2O_3 subcycles, respectively. The dotted lines in the figures illustrate the metal content expected from the rule of mixture formula[32]

$$\text{Sn content}(\%) = [\rho_{Sn} \times \%\ SnO_2/(\rho_{Sn} \times \%\ SnO_2 + \rho_{Al}(100 - \%\ SnO_2))] \times 100$$

where % SnO_2 is the percentage of SnO_2 subcycles and ρ_{Sn} and ρ_{Al} are the area densities of Sn and Al atoms per cycle in their pure oxide films, respectively. From the pure SnO_2 and Al_2O_3 films grown in the present study, ρ_{Sn} and ρ_{Al} were found to be 3.67 and 3.35 atoms/nm^2 per cycle, respectively. It is seen from Figure 3a that measured Sn content is below the dotted line predicted from the rule of mixture over the whole range. The Al content, on the other hand, is always higher than the expected value. The discrepancy becomes most apparent when the percentage of Al_2O_3 (also SnO_2) subcycles is close to 25% (75% for SnO_2), which corresponds to ~50 atom % of both Al and Sn.

The film composition using only SnO_2 cycles was measured to be SnO_x ($x = 2.0-2.1$) by RBS analysis. Its film density from RBS and XRR was 5.83 g/cm^3, or 83.4% of the bulk crystalline value for SnO_2 (6.99 g/cm^3). The large volume of grain boundaries appears to be one of the reasons for somewhat low film density compared to the ideal value.[36] The value is similar to other ALD−SnO_2 film (5.64 g/cm^3) reported by Du et al.[43] After a 350 °C anneal in nitrogen ambient for 1 h, the film density increased to ~6.0−6.1 g/cm^3. The Al_2O_3 film stoichiometry was AlO_x ($x = 1.5-1.6$), and its density was 2.83 g/cm^3, or 76.7% of the bulk crystalline value for Al_2O_3 (3.69 g/cm^3). This value of Al_2O_3 film corresponds well to the density trend depending on the growth temperature reported by Groner et al.[44]

Figure 3c shows the calculated film densities by using the total number of atoms counted by RBS and the film thicknesses obtained by XRR. The dotted line represents the expected densities predicted from the rule of mixture

$$\text{film density}(g/cm^3) = [\rho_{Al_2O_3} \times \%\ Al_2O_3 + \rho_{SnO_2} \times (100 - \%\ Al_2O_3)]/100$$

where $\rho_{Al_2O_3}$ and ρ_{SnO_2} are film densities of pure Al_2O_3 and SnO_2 films. It can be seen from Figure 3c that the actual density values deviate below the expected ones. The refractive indices also followed a similar trend (Table 1).

To understand the chemisorption behavior of each metal precursor, the relative atomic concentration of Sn and Al per growth subcycle is plotted in Figure 4. Each atomic concentration per subcycle was normalized by its own value, SnO_2 (3.67 atoms/nm^2) and Al_2O_3 (3.35 atoms/nm^2), respectively. As shown in Figure 4, the relative Sn concentration per cycle (closed squares) gradually decreases as the number of subcycles of SnO_2 decreases, which indicates initial retarded chemisorption of Sn precursor on Al_2O_3 surfaces. When the number of SnO_2 subcycles is 2 [60(2,3)], the average Sn concentration per cycle is only ~52% of pure SnO_2. By using the average chemisorption values of CAT on an Al_2O_3 surface, we were able to estimate the chemisorption amounts at the initial stages of SnO_2 growth on Al_2O_3: the first, second, and third chemisorptions of CAT on Al_2O_3 ranged from 30 to 50, 50−70, and 75−94%, respectively, compared to its chemisorption on SnO_2. Four to five incubation cycles were necessary before the CAT precursor increased its adsorption per cycle back to its usual amount on SnO_2 surface. Similar retarded chemisorption was reported for DEZ[32,33] and TTIP[30] following Al_2O_3 subcycles.

On the other hand, the chemisorption of TMA on SnO_2 surface (closed circles) is strongly enhanced, as shown in Figure 4. When one Al_2O_3 subcycle is used [i.e., l = 1, 12(24,1), 30(9,1), and 75(3,1)], about 2.16 times higher chemisorption (7.25 atoms/nm^2) of TMA per cycle was observed compared to its usual number of 3.35 atoms/nm^2 on Al_2O_3, which corresponds to ~76% of one monolayer of Al_2O_3 by one growth cycle.[22] Kim et al. reported about 1.6 times enhanced chemisorption of TMA on TiO_2 surfaces, which was measured by inductively coupled plasma atomic emission spectroscopy.[30] On ZnO surface, however, Elam et al.[32] and Na et al.[33] reported contrary chemisorption behavior of TMA although they both used the same Zn and Al precursors and in situ quartz crystal microbalance for elemental

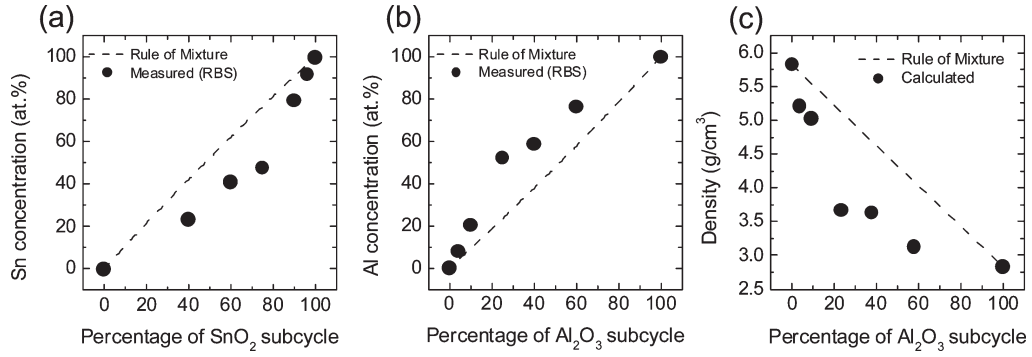

Figure 3. (a) Sn and (b) Al content (±1.5 atom %) measured from RBS analyses as a function of the percentage of SnO_2 and Al_2O_3 subcycle, respectively. Less Sn content was detected from RBS compared with the prediction from the rule of mixture (dotted lines) and vice versa for Al. (c) The film densities calculated using the concentrations of Sn, Al, and O atoms obtained from RBS analysis and the film thicknesses from XRR.

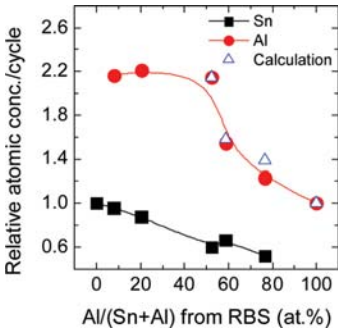

Figure 4. The relative cation concentration per unit area per cycle analyzed from RBS. The solid line is just for visual guidance. As the number of Al_2O_3 subcycles increase, the relative Sn concentration per cycle (closed squares, black color) gradually decreased. However, the relative Al concentration per cycle (closed circles, red color) stays at about 2.2 times higher than that of the undoped Al_2O_3 case (when the number of Al_2O_3 subcycles is 1) and then decreases when the Al concentration is higher than 50 atom %, where the number of Al_2O_3 subcycle is 2 or more. Open triangles (blue color) represent the calculated average values of relative Al concentrations per cycle if first subcycle is ~2.2 times enhanced and the next subcycles are all the same thickness as on pure Al_2O_3. The simulated values well match with the measured values, suggesting that the chemisorption of TMA after one Al_2O_3 subcycle on SnO_2 surface immediately recovers its own value for pure Al_2O_3.

quantification; Elam et al.[32] reported retarded chemisorption of TMA for two to three cycles on ZnO surface, whereas Na et al.[33] observed the same mass uptake of TMA on ZnO.

The enhanced chemisorption of TMA on SnO_2 surfaces remains relatively constant up to the point where the Al concentration of the composite film is ~50 atom % and then it starts to decrease as the Al concentration increases further. This corresponds to the experiments where either two or three subcycles of Al_2O_3 were used [60(3,2) and 60(2,3)] instead of one subcycle. For the second TMA−H_2O_2 subcycle on SnO_2, it appears that the Al_2O_3 growth recovers its original value of ~3.35 atoms/nm^2 per cycle. The sequences of 60(3,2) and 60(2,3), where the measured Al concentrations are 58.6 and 76.5 atom %, respectively, can be used to show this result. If the first and second/third Al_2O_3 subcycles on SnO_2 have chemisorptions of ~2.16 and 1, respectively, relative to their normal values on Al_2O_3, then the average chemisorption for two and three Al_2O_3 subcycles on SnO_2 should be 1.58 and 1.39, respectively. The measured values for these cases were 1.54 ± 0.08 and 1.23 ± 0.08, which matched reasonably well with the calculated values. This comparison suggests that after the first Al_2O_3 subcycle, which forms nearly one monolayer of Al_2O_3, subsequent chemisorption of TMA immediately returns to its original behavior like on pure Al_2O_3 surface. Thus the underlying SnO_2 surface is fairly completely covered by the first Al_2O_3 subcycle, so that the SnO_2 layer beneath does not influence the second Al_2O_3 subcycle.

On the basis of these observed chemisorption behaviors of CAT and TMA, an empirical model was derived to calculate the Al atomic concentration for each sequence. For chemisorption of CAT on Al_2O_3, the first SnO_2 subcycle deposited 40% of its usual amount on SnO_2 surfaces. The second deposited 60%, the third 80%, the fourth 90%, and subsequent SnO_2 subcycles gave 100% of the usual growth on SnO_2. For chemisorption of TMA on SnO_2, the first subcycle deposited 216% of the amount normally deposited on Al_2O_3, and subsequent Al_2O_3 subcycles deposited 100% of the usual amount on Al_2O_3. The compositions calculated in this way are fairly well matched with the measured values (Table 1).

One of the possible factors that affect the amount of TMA chemisorption is how rough the underlying surface is prior to a TMA−H_2O_2 subcycle. Large surface roughness, i.e., large surface area, could lead to higher chemisorption of TMA per one cycle on a SnO_2 surface. To study whether the surface area plays an important role for the enhanced chemisorption, surface roughness of the films was measured by AFM after the deposition. Panels a−d of Figure 5 show the surface morphologies of SnO_2 [556(1,0)], 7.9 atom % Al−SnO_x [30(24,1)], 20.4 atom % Al−SnO_x [60(9,1)], and Al_2O_3 films [910(0,1)], respectively. To eliminate the thickness effect and enhance the distinction among samples, the final film thickness of all samples was set to be ~100 nm. Figure 5e summarizes its root-mean-square roughness (R_s) of those samples. The R_s of the SnO_2 film was 3.2 nm. Interestingly, a drastic drop in R_s of the (Sn,Al)O_x films to 0.45−0.50 nm was observed. The roughness of undoped Al_2O_3 was similar (0.55 nm). This result indicates that repetitive Al_2O_3 incorporation effectively suppresses the further growth of SnO_2 grains, resulting in smaller grain size than that of SnO_2. On the basis of these roughness values, it can be inferred that, when TMA injection occurs, the surface area of SnO_2 should not be much larger than that of the pure SnO_2. Thus a larger surface area cannot explain the higher adsorption of TMA on SnO_2.

It is known that a higher density of hydroxyl groups leads to increased chemisorption of TMA on Al_2O_3.[22] To compare the

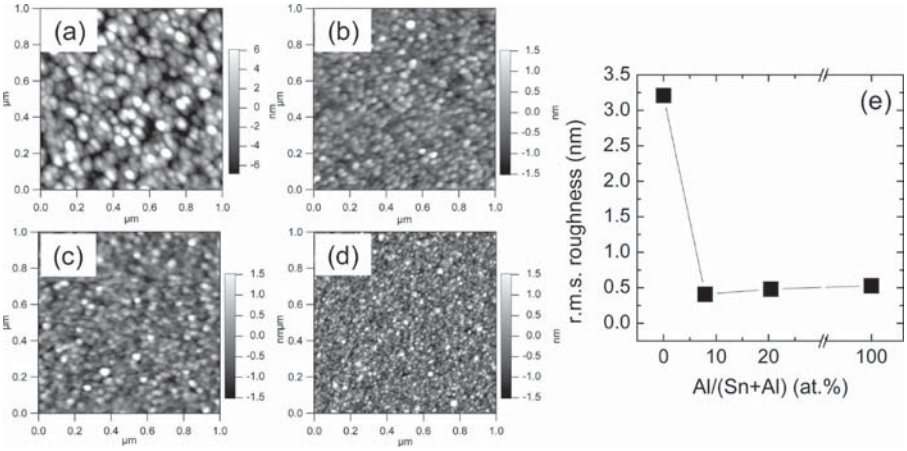

Figure 5. Surface morphologies of (a) SnO_2 [556(1,0)], (b) 7.9 atom % Al−SnO_x [30(24,1)], (c) 20.4 atom % Al−SnO_x [60(9,1)], and (d) Al_2O_3 [910(0,1)] observed by AFM. Total repetition (m) of each sample was set to make the film thickness to ~100 nm. (e) The root-mean-square roughness (R_s) as a function of Al concentration of the films. A drastic drop in R_s from 3.2 (a) to 0.41 nm (b) was observed when one subcycle of Al_2O_3 was inserted into SnO_2. The R_s values are very small (less than 0.5 nm) for the (Sn,Al)O_x composite films (b, c), as well as for Al_2O_3 (d).

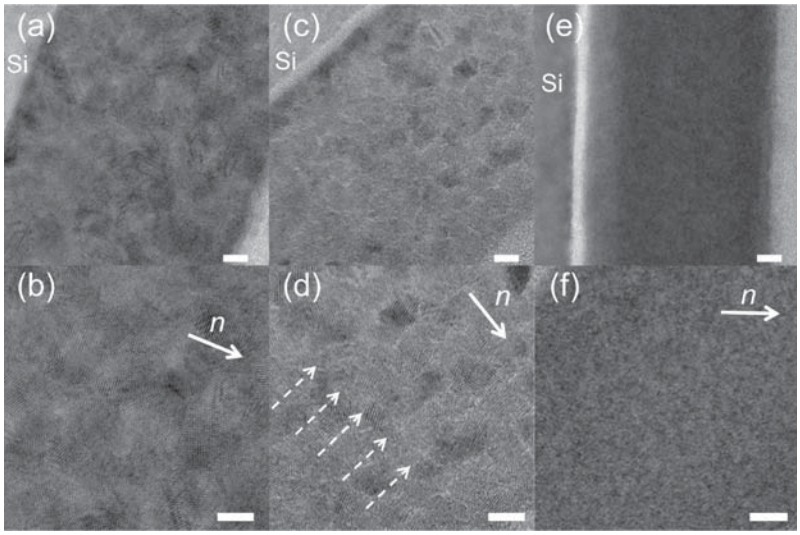

Figure 6. Cross-sectional TEM images of (a, b) undoped SnO_2,[36] (c, d) 7.9 atom % Al−SnO_x, and (e, f) 52.3 atom % (Al,Sn)O_x films. All scale bars represent 5 nm. The direction normal to the Si substrate (n) is noted with an arrow. Both undoped and 7.9 atom % Al−SnO_x are polycrystalline. However, the nucleation of undoped SnO_2 is random while the grains of 7.9 atom % Al−SnO_x appear to align on one plane which is parallel to the substrate. It is seen from panel c that the number of the stacks of SnO_2 grains is 12, which is the repetition (m) used in 12(24,1) sequence. Dotted arrows of panel d indicate the partially amorphous Al_2O_3 layers with brighter contrast than SnO_2 grains. (e, f) 52.3 atom % (Al,Sn)O_x film is amorphous. Somewhat thicker native SiO_2 layer (2−3 nm) may be due to the beam damage during the sample preparation.

density of hydroxyl groups on ALD SnO_2 and Al_2O_3 films, static water contact angle measurements were performed. A lower contact angle corresponds to a higher density of hydroxyl groups. The contact angles of SnO_2 and Al_2O_3 were 33 ± 1° and 47 ± 2°, respectively. Thus the SnO_2 surface appears to contain a higher density of hydroxyl groups than Al_2O_3 does, which correlates with its higher adsorption of TMA. However, this relatively small difference in the contact angles of SnO_2 and Al_2O_3 does not fully account for the highly enhanced chemisorption of TMA on a SnO_2 surface.[45] One of the possible contributing factors is the diffusion of Al ions during the TMA exposure like the TiO_2 case where the retarded chemisorption of the Ti precursor was also reported by Kim et al.[30,31] More detailed study is needed to clarify the origin of the enhanced chemisorption of TMA on a SnO_2 surface.

Cross-sectional TEM was used to study how Al_2O_3 subcycle affects the microstructure of the growing films. Panels a and b of Figure 6 show the cross-sectional TEM images[36] of SnO_2 grown for the same total growth cycles for comparison (scale bar, 5 nm). From the higher magnification image shown in Figure 6b, it is seen that SnO_2 grows as a polycrystalline phase (rutile structure) and its grain size varies roughly from 5 to 10 nm.[36] It is seen that crystalline grains overlap with each other, which indicates that nucleation and growth of SnO_2 grains occurs somewhat in random directions as the film grows. Panels c and d of Figure 6 show the cross-sectional TEM images of 7.9 atom % Al−SnO_x film [12(24,1)] with the same magnification. The film thickness was about 50 nm, and its nominal growth rate was calculated to be 0.166 nm/cycle, a little smaller than that of SnO_2, which is

0.175 nm/cycle. The observed average grain size of 7.9 atom % Al−SnO_x is ∼4−5 nm, which is smaller than that of pure SnO_2 (Figure 6b). The average grain size observed in these images is similar to the thickness roughly expected from the number of SnO_2 subcycles (24 cycles) and its growth rate (0.175 nm/cycle). Notably, the distribution of grain sizes is narrower than that of SnO_2. This indicates that one additional Al_2O_3 subcycle for every 24 subcycles of SnO_2 inhibits the further growth of pre-existing SnO_2 grains. This result suggests that even one subcycle of TMA−H_2O_2 effectively screens underlying SnO_2 crystallites, which is reasonable based on the enhanced chemisorption of TMA on SnO_2 surface. The low roughness of these films can also be explained by this observation. Similarly, Elam et al. observed a renucleation of the ZnO crystal growth on a Al_2O_3 layer in a ZnO/Al_2O_3 nanolaminate system.[46]

From Figure 6d, it is also noted that SnO_2 crystallites form side-by-side on a plane normal to the growth direction. The thin amorphous layers observed between the SnO_2 layers are expected to be Al_2O_3 or Al−O−Sn.[33] The number of those amorphous layers is 11, which is consistent with the total number of subcycles of TMA−H_2O_2 except for the last subcycle, which is not distinguishable from the top glue layer. This parallel nucleation and growth of SnO_2 crystallites observed from the TEM images indicates that even one subcycle of TMA−H_2O_2 blocks the crystalline information of SnO_2 underneath and that Al atoms are not homogeneously mixed with SnO_2. A similar periodic peak-and-valley distribution of Al along the growth direction was also reported in ALD Al-doped ZnO by using secondary ion mass spectrometry[33] and cross-sectional TEM.[37]

The 20.4 atom % Al−SnO_x film [30(9,1)] was still polycrystalline like the 7.9 atom % Al−SnO_x film (image not shown). However, distinct amorphous layers were not clearly distinguishable for this sample, which appears to be reasonable considering the expected thickness (<∼1.5 nm) of the SnO_2 layers between the Al_2O_3 layers. Panels e and f of Figure 6 show the cross-sectional TEM images of 52.3 atom % (Al,Sn)O_x film [75(3,1)]. Unlike SnO_2 and 7.9 atom % Al-doped SnO_x cases, the microstructure of the film turned out to be amorphous. On the basis of the TEM results, the microstructural transition of (Sn,Al)O_x composite films occurs between 20.4 and 52.3 atom % of Al. The thicknesses of 20.4 and 52.3 atom % Al−SnO_x films were ∼38−40 nm, which correspond to the nominal growth rate of ∼0.13 nm/cycle. As the percentage of Al_2O_3 subcycle increases, the nominal growth rate decreases and approaches to the growth rate of Al_2O_3 (0.10 nm/cycle).

The inhomogeneous distribution of Al in SnO_2 was further investigated by electrical measurements. $I-V$ measurements were carried out to evaluate the resistance to electron flow through the film perpendicular to its surface. Four point probe measurement was used to find the resistivity in the lateral direction, but the measurement limit was low (<10^6 Ω/square). Thus, only samples with Al concentrations less than 10% could be measured in this way. Therefore, the circular transmission line method,[40,41] which provides a higher measurement limit (∼10^{10} Ω/square), was also used to study lateral electron flow parallel to the surface of the film.

Figure 7a summarizes the observed resistivity of films with various Al concentrations. Here, closed circles and open squares represent resistivity measured perpendicular through the film and laterally (parallel) to the film surface, respectively. Even a small amount of Al incorporated into the SnO_2 films [12(24,1)]

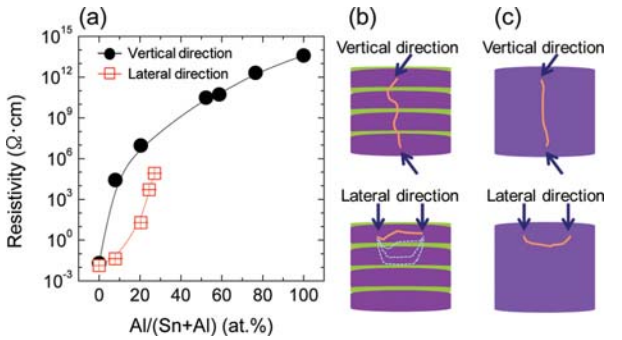

Figure 7. (a) The calculated resistivity as a function of atomic concentrations of Al for perpendicular current flow (closed circles) and lateral current flow (open squares). (b) Thin layers of green color represent Al_2O_3 (or Al−O−Sn) layers. Thick layers of violet color represent conducting SnO_2 layers. The schematic explains why large anisotropy in resistivities happens at low concentrations of Al. (c) The schematic illustrates a homogeneous, amorphous mixture of Al_2O_3 and SnO_2 that forms at higher Al concentrations, which explains the convergence of resistivity values for the two directions.

causes a drastic increase of resistivity measured through the film. This result suggests that even one subcycle of Al_2O_3 can dramatically interrupt the vertical electron flow in SnO_2 (Figure 7b). On the other hand, the same amount of Al content causes only a small increase in resistivity measured laterally along the plane of the film by the circular transmission line method. The lateral resistivity measured by the circular transmission line method is plotted only up to ∼10^6 Ω·cm due to limitations of the measurement. As the Al concentration increases further, the resistivity in perpendicular direction eventually approaches to that of pure Al_2O_3 (∼4 × 10^{13} Ω·cm). The resistivity in the lateral direction shows a much slower increase compared to the resistivity in the perpendicular direction. The slow increase in lateral resistivity appears to come from the increased scattering of electrons due to smaller grain sizes observed in TEM images (Figure 6c,d) as well as the decreased portion of conducting SnO_2.

The 2 to 6 order of magnitude difference in resistivities parallel and perpendicular to the film may be attributed to the inhomogeneous distribution of resistive Al_2O_3 between the conductive SnO_2 layers. In the case of lateral electron flow, current can flow through conductive SnO_2 layers instead of resistive Al_2O_3 (or Al−Sn−O) layers. For current flowing perpendicular to the film, however, electrons inevitably flow multiple times through the highly resistive Al_2O_3 (or Al−Sn−O) layers, leading to a drastic increase in resistivity through the film (Figure 7b). Such anisotropic electrical properties have not been reported for sputter-processed films where a homogeneous mixture of Al and Sn is expected.[11]

As the Al concentration increases over ∼20 atom %, the lateral resistivity quickly approaches toward the vertical resistivity, as shown in Figure 7a. The actual convergence of those two values could not be observed because of the detection limit of the circular transmission line method. On the basis of the trend of those two plots, however, they are expected to show close values for films with Al concentration higher than ∼35 atom % due to the more homogeneous nature of the films (Figure 7c). This result is consistent with the TEM observation, where the phase change from crystalline to amorphous state occurred between 20 and 50 atom % Al−SnO_x.

IV. CONCLUSIONS

We studied macroscopic properties of $(Sn,Al)O_x$ composite films, such as density, crystallinity, refractive index, resistivity, roughness, as well as growth rate of each layer, depending on the number of subcycles of Al_2O_3 and SnO_2. By using RBS analyses, the chemisorption behaviors of the aluminum precursor TMA and the Sn precursor CAT were determined. The chemisorption of TMA on SnO_2 surface showed a large enhancement compared to the case of pure Al_2O_3. After the first Al_2O_3 subcycle, however, the chemisorption of TMA decreased to its original rate after the formation of almost a complete monolayer of Al_2O_3. In contrast, the chemisorption of the Sn precursor on Al_2O_3 was greatly retarded and took several cycles to increase back to its usual value on SnO_2. These differences were related to the observation that SnO_2 surface is more hydrophilic than the Al_2O_3 surface. Highly anisotropic electrical properties of the nanolaminate $(Sn,Al)O_x$ films were revealed by comparing $I-V$ and circular transmission line measurements of nanolaminate films. As more aluminum was added, the microstructure changed from nanocrystalline nanolaminate to amorphous, and the anisotropy in the resistivity tended toward zero. By changing the number of SnO_2 and Al_2O_3 subcycles, the resistivity could be adjusted over 15 orders of magnitude. Detailed study of the chemisorption properties of different precursors can provide insight into the formation and composition of multicomponent materials grown by ALD.

AUTHOR INFORMATION

Corresponding Author

*E-mail: gordon@chemistry.harvard.edu.

ACKNOWLEDGMENT

The authors thank Dr. Adam S. Hock for synthesizing the Sn precursor. We appreciate discussions with Dr. Philippe de Rouffignac. This work was performed in part at the Center for Nanoscale Systems (CNS) at Harvard University, a member of the National Nanotechnology Infrastructure Network (NNIN), which is supported by the National Science Foundation under NSF award no. ECS-0335765.

REFERENCES

(1) Hartnagel, H. L.; Dawar, A. L.; Jain, A. K.; Jagadish, C. *Semiconducting Transparent Thin Films*; IOP: Bristol, U.K., 1995.
(2) Minami, T. *Semicond. Sci. Technol.* **2005**, *20*, S35–S44.
(3) Gordon, R. G. *MRS Bull* **2000**, *25*, 52–57.
(4) Gordon, R. G. *US Patent* 4,265,974, 1981.
(5) Proscia, J.; Gordon, R. G. *Thin Solid Films* **1992**, *214*, 175–187.
(6) Gordon, R. G. *Mater. Res. Soc. Symp. Proc.* **1996**, *426*, 419–429.
(7) Gordon, R. G.; Proscia, J.; Ellis, F. B.; Delahoy, A. E. *Sol. Energy Mater.* **1989**, *18*, 263–281.
(8) Gordon, R. G. *J. Non-Cryst. Solids* **1997**, *218*, 81–91.
(9) Chiang, H. Q.; Wager, J. F.; Hoffman, R. L.; Jeong, J.; Keszler, D. A. *Appl. Phys. Lett.* **2005**, *86*, 013503.
(10) Presley, R. E.; Munsee, C. L.; Park, C.-H.; Hong, D.; Wager, J. F.; Keszler, D. A. *J. Phys. D: Appl. Phys.* **2004**, *37*, 2810–2813.
(11) Huh, M. S.; Yang, B. S.; Oh, S.; Lee, J.; Yoon, K.; Jeong, J. K.; Hwang, C. S.; Kim, H. J. *Electrochem. Solid-State Lett.* **2009**, *12*, H385–H387.
(12) Govyadinov, A.; Emeliantchik, I.; Kurilin, A. *Nucl. Instrum. Methods Phys. Res., Sect. A* **1998**, *419*, 667–675.
(13) Beaulieu, D. R.; Gorelikov, D.; de Rouffignac, P.; Saadatmand, K.; Stenton, K.; Sullivan, N.; Tremsin, A. S. *Nucl. Instrum. Methods Phys. Res., Sect. A* **2009**, *607*, 81–84.
(14) Drobychev, G.; Barysevich, A.; Delendik, K.; Nédélec, P.; Sillou, D.; Voitik, O. *Nucl. Instrum. Methods Phys. Res., Sect. A* **2009**, *610*, 246–248.
(15) Kim, J. Y.; Lee, K.; Coates, N. E.; Moses, D.; Nguyen, T.-Q.; Dante, M.; Heeger, A. J. *Science* **2007**, *317*, 222–225.
(16) Suntola, T. *Thin Solid Films* **1992**, *216*, 84–89.
(17) Leskelä, M.; Ritala, M. *Angew. Chem., Int. Ed.* **2003**, *42*, 5548–5554.
(18) George, S. M. *Chem. Rev.* **2009**, *110*, 111–131.
(19) Leskelä, M.; Ritala, M. *Thin Solid Films* **2002**, *409*, 138–146.
(20) George, S. M.; Ott, A. W.; Klaus, J. W. *J. Phys. Chem.* **1996**, *100*, 13121–13131.
(21) Gordon, R. G.; Hausmann, D.; Kim, E.; Shepard, J. *Chem. Vap. Deposition* **2003**, *9*, 73–78.
(22) Puurunen, R. L. *J. Appl. Phys.* **2005**, *97*, 121301.
(23) Farmer, D. B.; Gordon, R. G. *Nano Lett.* **2006**, *6*, 699–703.
(24) Xuan, Y.; Wu, Y. Q.; Shen, T.; Qi, M.; Capano, M. A.; Cooper, J. A.; Ye, P. D. *Appl. Phys. Lett.* **2008**, *92*, 013101.
(25) Choi, B. J.; Jeong, D. S.; Kim, S. K.; Rohde, C.; Choi, S.; Oh, J. H.; Kim, H. J.; Hwang, C. S.; Szot, K.; Waser, R.; Reichenberg, B.; Tiedke, S. *J. Appl. Phys.* **2005**, *98*, 033715.
(26) Kim, J.-H.; Kim, J.-Y.; Kang, S.-W. *J. Appl. Phys.* **2005**, *97*, 093505.
(27) Hwang, G. W.; Lee, H. J.; Lee, K.; Hwang, C. S. *J. Electrochem. Soc.* **2007**, *154*, G69–G76.
(28) Lee, S. W.; Kwon, O. S.; Han, J. H.; Hwang, C. S. *Appl. Phys. Lett.* **2008**, *92*, 222903.
(29) Elam, J. W.; Routkevitch, D.; George, S. M. *J. Electrochem. Soc.* **2003**, *150*, G339–G347.
(30) Kim, S. K.; Choi, G. J.; Kim, J. H.; Hwang, C. S. *Chem. Mater.* **2008**, *20*, 3723–3727.
(31) Kim, S. K.; Choi, G.-J.; Lee, S. Y.; Seo, M.; Lee, S. W.; Han, J. H.; Ahn, H.-S.; Han, S.; Hwang, C. S. *Adv. Mater.* **2008**, *20*, 1429–1435.
(32) Elam, J. W.; George, S. M. *Chem. Mater.* **2003**, *15*, 1020–1028.
(33) Na, J.-S.; Peng, Q.; Scarel, G.; Parsons, G. N. *Chem. Mater.* **2009**, *21*, 5585–5593.
(34) Yousfi, E. B.; Weinberger, B.; Donsanti, F.; Cowache, P.; Lincot, D. *Thin Solid Films* **2001**, *387*, 29–32.
(35) Elam, J. W.; Baker, D. A.; Hryn, A. J.; Martinson, A. B. F.; Pellin, M. J.; Hupp, J. T. *J. Vac. Sci. Technol., A* **2008**, *26*, 244–252.
(36) Heo, J.; Hock, A. S.; Gordon, R. G. *Chem. Mater.* **2010**, *22*, 4964–4973.
(37) Lee, D.-J.; Kim, H.-M.; Kwon, J.-Y.; Choi, H.; Kim, S.-H.; Kim, K.-B. *Adv. Funct. Mater.* **2011**, *21*, 448–455.
(38) Elam, J. W.; Groner, M. D.; George, S. M. *Rev. Sci. Instrum.* **2002**, *73*, 2981–2987.
(39) Kumagai, H.; Matsumoto, M.; Kawamura, Y.; Toyoda, K.; Obara, M. *Jpn. J. Appl. Phys.* **1994**, *33*, 7086–7089.
(40) Hewett, C. A.; Taylor, M. J.; Zeidler, J. F.; Geis, M. W. *J. Appl. Phys.* **1995**, *77*, 755–760.
(41) Bierwagen, O.; White, M. E.; Tsai, M.-Y.; Nagata, T.; Speck, J. S. *Appl. Phys. Express* **2009**, *2*, 106502.
(42) Banerjee, A. N.; Maity, R.; Kundoo, S.; Chattopadhyay, K. K. *Phys. Status Solidi A* **2004**, *201*, 983–989.
(43) Du, X.; George, S. M. *Sens. Actuators, B* **2008**, *135*, 152–160.
(44) Groner, M. D.; Fabreguette, F. H.; Elam, J. W.; George, S. M. *Chem. Mater.* **2004**, *16*, 639–645.
(45) Seki, K.; Tachiya, M. *J. Phys. Chem. B* **2004**, *108*, 4806–4810.
(46) Elam, J. W.; Sechrist, Z. A.; George, S. M. *Thin Solid Films* **2002**, *414*, 43–55.